

1 **Mechanism of formation, characterization and cytotoxicity of**
2 **green synthesized zinc oxide nanoparticles obtained from *Ilex***
3 ***paraguariensis* leaves extract**

4

5

6

7

8 *Marina Bandeira^{a,c}, André L. Possan^a, Sandra S. Pavin^b, Camila S. Raota^a, Mario C.*9 *Vebber^a, Marcelo Giovanela^a, Mariana Roesch-Ely^b, Declan M. Devine^c*10 *and Janaina da S. Crespo^{a,*}*

11

12

13

14

15 ^aUniversidade de Caxias do Sul, Rua Francisco Getúlio Vargas, 1130, Caxias do Sul,

16 95070-560, RS, Brazil

17 ^bInstituto de Biotecnologia, Universidade de Caxias do Sul, Rua Francisco Getúlio

18 Vargas, 1130, Caxias do Sul, 95070-560, RS, Brazil

19 ^cMaterials Research Institute, Athlone Institute of Technology, Athlone, Co.

20 Westmeath, Ireland

21

22

23

24

Phone/Fax: + 55 54 32182159 / *Corresponding author. E-mail : jscrespo@ucs.br

25 **ABSTRACT**

26 Zinc oxide nanoparticles (ZnONPs) was produced using *Ilex paraguariensis* (mate)
27 leaves extract using a green synthesis process. The influence of ethanolic and aqueous
28 plant extract and zinc source on the green synthesis of ZnONPs was studied. Cyclic
29 voltammetry and Fourier transform infrared spectroscopy (FTIR) were used for the
30 assessment of the mechanism route of ZnONPs while the formation of this nanomaterial
31 was confirmed by X-ray diffraction (XRD) analysis. The morphology and size of the
32 ZnONPs synthesized were evaluated using field emission scanning microscopy (FESEM)
33 and transmission electron microscopy (TEM) analysis. In general, all different
34 synthesized ZnONPs exhibited a hexagonal crystalline structure whereas the size and
35 shape varied depending on the extract and zinc salt used. Nonetheless, the most uniform
36 and smallest ZnONPs were obtained using ethanolic extract and zinc nitrate, showing
37 spherical morphology and a diameter of about 18 nm. With the use of cyclic voltammetry
38 and FTIR analysis, it was concluded that the formation of ZnONPs through green
39 synthesis occurred due to complexation of Zn(II) ions by antioxidants compounds present
40 in the *Ilex paraguariensis* extract and further thermal degradation of the complexes.
41 Concerning the cytotoxicity assays, the L929 cell viability decreases in a dose-dependent
42 manner for all samples tested. In general, nanoparticles with reduced size and uniform
43 shape exhibited no cytotoxic effects up to a concentration of 10 $\mu\text{g mL}^{-1}$. However, higher
44 ZnONPs concentrations caused a decrease in cell viability. This was possibly due an
45 autophagic induction process triggered by the internalization of the nanomaterial. Finally,
46 this work provides a better understanding of the mechanism route to obtain ZnONPs *via*
47 green method and their potential to be used as a biomedical material.

48 **Keywords:** *Ilex paraguariensis*; green synthesis; zinc oxide nanoparticles; mechanism
49 route; cytotoxicity

50 **1 INTRODUCTION**

51

52 Nanotechnology is a growing field of science and researchers believe that the use
53 of nanomaterials will increase considerably in a variety of subjects [1–4]. Within this
54 context, zinc oxide nanoparticles (ZnONPs) have been widely investigated due to their
55 unique physical, chemical and optical properties that enables them to be utilized in a
56 variety of technological applications, including novel biomedical devices and therapies
57 [5–8]. More specifically, ZnONPs enhanced the efficacy of bone regeneration when
58 incorporated to polymer scaffolds by inducing early mineralization and preventing
59 infections due its antibacterial activity [9]. This nanomaterial has also been investigated
60 for its wound healing performance. The incorporation of ZnONPs on polymeric beads,
61 for example, led to faster wound closure and avoided the formation of microbial biofilms
62 on the skin [10]. This characteristics corroborates with the findings of related studies [11–
63 15].

64 The toxicity of ZnONPs for use in human health applications is still a subject of
65 discussion, as nanomaterials have different toxicity mechanism routes, such as reactive
66 oxygen species (ROS) production, cell internalization and metal ions release, among
67 others, which can affect human cells in different manners compared to the bulk material
68 form [16]. Recent developments on this topic have been made, and the cytotoxicity of
69 oxide nanoparticles are now known to be not only dose-dependent, but also associated
70 with properties like size, morphology and surface characteristics [17–19].

71 Several methods are applied to obtain these nanomaterials through chemical,
72 physical or biological synthesis [20,21]. However, the biological approach has gained
73 much attention as it is more environmentally friendly than conventional methods,
74 considering that it substitutes hazardous solvents by plant extracts, and can improve the

75 properties of the nanomaterials. Commonly known as green synthesis, many plant
76 extracts have been used to synthesize metal and metal oxides nanoparticles with enhanced
77 properties [22–30]. Although the mechanism of formation of nanoparticles through green
78 synthesis is not completely understood, it is believed that antioxidant compounds present
79 in the plant, such as flavonoids and polyphenols, reduce or form coordinated complexes
80 with the targeted metal [31–33].

81 Many plant extracts have been applied to the green synthesis of ZnONPs
82 [26,32,34–37]. Gunalan et al. [38], for example, used *Aloe vera* extract and obtained
83 ZnONPs with enhanced antibacterial effect in comparison to ZnONPs synthesized by
84 chemical method. Shahriyari Rad et al. [39] also confirmed the antimicrobial activity of
85 ZnONPs obtained using *Menta pulegium L* leaves. Nava et al. [31] obtained ZnONPs
86 using fruit peel extract for photocatalytic degradation of dyes with enhanced degradation
87 rate than ZnONPs commercially available.

88 In this work, we report the green synthesis of ZnONPs and its optimization using
89 *Ilex paraguariensis* leaves extract. This plant, also called *mate*, is commonly found in the
90 south of Brazil, Uruguay and Argentina, where it is used to prepare a traditional tea [40].
91 Anxiolytic, neuroprotective and anti-inflammatory properties have been described in
92 *mate* tea and have been associated to a variety of antioxidant compounds found in the
93 plant, which includes chlorogenic acid, caffeic acid and caffeine [41–43].

94 Although many tea extracts have been used for synthesizing ZnONPs [44–46], to
95 the best of our knowledge, the use of *Ilex paraguariensis* leaves to obtain ZnONPs has
96 not been reported in the literature. In addition, even though much research has designed
97 a probable mechanism route for the green synthesis, none have used cyclic voltammetry
98 to evaluate and confirm it. In this sense, this work contributes to a better understanding
99 of the green synthesis of ZnONPs in a molecular level, which is essential to develop and

100 implement a sustainable large-scale production of nanoparticles. Moreover, a carefully
101 study on the cytotoxicity and cell internalization of ZnONPs was performed to evaluate
102 their application in the biomedical field.

103

104 **2 MATERIALS**

105 The materials used to perform the green synthesis include zinc nitrate hexahydrate
106 (Sigma-Aldrich, São Paulo, Brazil), zinc acetate dihydrate (Sigma-Aldrich, São Paulo,
107 Brazil) and ethanol 99% (Didática Artigos para Laboratório Ltda, São Paulo, Brazil). The
108 *Ilex paraguariensis* leaves were collected in the municipality of Caxias do Sul (Rio
109 Grande do Sul, Brazil) and identified at the Natural Science Museum of University of
110 Caxias do Sul (registration number 46.334).

111 For the characterization of the leaves extract Folin Ciaocalteau 2N (Didática
112 Artigos para Laboratório Ltda, São Paulo, Brazil), calcium carbonate P.A. (Didática
113 Artigos para Laboratório Ltda, São Paulo, Brazil), trishydrochloride (Sigma-Aldrich, São
114 Paulo, Brazil) and 1,1-diphenyl-2-picrylhydrazyl (DPPH, Sigma-Aldrich, São Paulo,
115 Brazil) were used.

116 Regarding the cellular tests the following materials were used: mouse fibroblast
117 L929 cells, cell medium Dulbecco's Modified Eagle's Medium (DMEM, Sigma-Aldrich,
118 São Paulo, Brazil), fetal bovine serum (FBS, Sigma-Aldrich, São Paulo, Brazil),
119 penicillin-streptomycin (P/S, Gibco, Thermo Fisher Scientific, Waltham, MA, United
120 States of America), 3-(4,5-dimethylthiazol-2-yl)-2,5-diphenyltetrazolium bromide
121 (MTT, Sigma-Aldrich, São Paulo, Brazil), dimethyl sulfoxide (DMSO, Sigma-Aldrich,
122 São Paulo, Brazil), Giemsa staining (Sigma-Aldrich, São Paulo, Brazil), rapamycin
123 (Sigma-Aldrich, São Paulo, Brazil), methanol (Sigma-Aldrich, São Paulo, Brazil),
124 monoclonal anti-LC3A/B antibody (autophagy kit, Cell Signaling, Danvers, MA, United

125 States of America), anti-mouse fluorescein isothiocyanate (FITC, Sigma-Aldrich, San
126 Luis, MO, United States of America) and bovine serum albumin (BSA, Sigma-Aldrich,
127 São Paulo, Brazil).

128

129 **3 METHODS**

130

131 *3.1 Ilex paraguariensis leaves extract preparation*

132 The *mate* leaves were cleaned carefully with the following sequence of rinses to
133 remove impurity particles: tap water, 50% (v/v) ethanol/water solution and distilled water,
134 respectively. Subsequently, the leaves were submitted to 60 °C for 1.5 h and were ground
135 in a mill. The ground leaves were stored in an amber flask under refrigeration (4 °C) for
136 further use.

137 To obtain the plant extract, 100 g L⁻¹ of the ground *mate* leaves were heated and
138 stirred with two different solvents: distilled water and a 50% (v/v) ethanol/water solution.
139 Three ranges of temperature (25 °C, 50 °C and 100 °C) and time of extraction (10 min,
140 20 min and 30 min) were evaluated, respectively. The extract was then filtered and
141 centrifuged for 20 min at 5,000 rpm to remove particles of the medium.

142

143 *3.2 Green synthesis of zinc oxide nanoparticles*

144 Zinc salt (nitrate and acetate) in a Zn(II) concentration of 21.8 g L⁻¹ was added to
145 50 mL of the *mate* extract previously prepared. The solution was stirred for 1 h at room
146 temperature and then heated for 4 h at 70 °C. After that, the mixture was submitted to a
147 hot air oven at 140 °C for 1 h, being finally calcinated at 400 °C for 1 h. The resulting
148 powder was collected for further characterization.

149 To evaluate the effect of the *mate* extract on the synthesis of ZnONPs, two samples
150 containing only zinc nitrate hexahydrate (named Nitrate) and zinc acetate dihydrate

151 (named Acetate) were calcinated under the same conditions used in the green synthesis
 152 (at 400 °C for 1 h). **Table 1** describes the synthesized ZnONPs samples and their
 153 conditions. Only the sample prepared with zinc nitrate and ethanolic extract (Nit_EtOHa)
 154 produced ZnONPs without calcination.

155

156 **Table 1** Description of the synthesized ZnONPs samples

| Sample | Zinc source | Plant extract solvent | Heat treatment |
|----------------------|--------------|-----------------------|----------------|
| Nitrate | | – | C |
| Nit_H ₂ O | Zinc nitrate | H ₂ O | O + C |
| Nit_EtOH | | 50% (v/v) EtOH | O + C |
| NIt_EtOHa | | 50% (v/v) EtOH | O |
| Acetate | | – | C |
| Act_H ₂ O | Zinc acetate | H ₂ O | O + C |
| Act_EtOH | | 50% (v/v) EtOH | O + C |

157 C = calcination; O = hot air oven

158

159 *3.3 Characterization of the mate leaves extract*

160 The antioxidant activity (AA) of the *mate* leaves extracts was evaluated through
 161 an oxidation-reduction reaction of the free radical 1,1-diphenyl-2-picrylhydrazyl (DPPH),
 162 following the method described by Yamaguchi et al. with slight modifications [47]. To
 163 perform the analysis, 100 µL of the plant extract was added to 400 µL of trishydrochloride
 164 0.1 mol L⁻¹ (pH = 7.0) and 500 µL of a DPPH 0.5 mmol L⁻¹ solution. The control sample
 165 was prepared with the substitution of the plant extract by its solvent (water or
 166 50 % (v/v) ethanol/water solution). After 20 min of incubation in the absence of light, the
 167 absorbance was measured in a UV-Vis spectrophotometer (Thermo Scientific, model
 168 Evolution 60, Waltham, MA, United States of America) at 517 nm.

169 The total polyphenolic content was determined following the procedure of
 170 Singleton and Rossi with adaptations [48]. For this, 150 µL of the plant extract was added

171 to 750 μL of Folin-Ciocalteu 10% (v/v) reagent and 600 μL of calcium carbonate 7.5%
172 (w/v). The mixture was slightly hand-shaken and incubated at 55 $^{\circ}\text{C}$ for 5 min. Then, at
173 room temperature, the absorbance was measured in a UV-Vis spectrophotometer
174 (Thermo Scientific, model Evolution 60, Waltham, MA, United States of America) at
175 760 nm. Total phenolic content was determined by comparison with a standard curve of
176 gallic acid (5, 25, 50, 75 and 100 $\mu\text{g mL}^{-1}$) and expressed in terms of micrograms of gallic
177 acid per milliliter of plant extract ($\mu\text{g EAG mL}^{-1}$).

178 The content of six main *mate* constituents was evaluated by high performance
179 liquid chromatography (HPLC, HP model 1100, Waldbronn, Germany), equipped with a
180 UV detector operating at 272 nm, a column Lichrospher RP18 5 μm and a quaternary
181 pumping system. Prior to the analysis, *mate* extracts were filtered through a Millipore
182 membrane (0.45 μm). The analysis in reverse phase mode was constituted of solvent A
183 (Milli-Q water and 1% (v/v) acetic acid) and solvent B (methanol). The mobile phase was
184 pumped with 75% of solvent A at 0.4 mL min^{-1} flux and the column was kept at 40 $^{\circ}\text{C}$
185 [49]. For the quantitative evaluation, a standard calibration curve was obtained using
186 standard solutions with a known concentration of the pure compounds (chlorogenic acid,
187 caffeic acid, theophylline, theobromine, rutin and caffeine).

188

189 *3.4 Evaluation of the green synthesis mechanism*

190 *3.4.1 Cyclic voltammetry*

191 ZnONPs synthesis mechanism was investigated through cyclic voltammetry using
192 a conventional three electrode cell at room temperature and a potentiostat (Ivium
193 Technologies, model Compactstat.h, Eindhoven, The Netherlands), operating with a
194 potential range from -1.7 V to 0.0 V , scanning speed of 50 mV s^{-1} and 1.0 mV step. Cyclic
195 voltammograms were obtained with a 3.0 mm glassy carbon working electrode, a

196 platinum wire as a counter electrode, an Ag/AgCl reference electrode and KCl
197 0.1 mol L⁻¹ as the electrolyte solution. The working electrode was polished with alumina
198 powder and cleaned with acetone in a 5 min ultrasonic bath prior to each analysis. The
199 peak current of the reduction or oxidation reaction is given according to the Rendles-
200 Sevcik equation (**Equation 1**):

201

$$i_p = 2,69 \times 10^5 n^{3/2} A D_0^{1/2} C_o v^{1/2} \quad (1)$$

202

203 where,

204 i_p = peak current (A);205 n = number of electrons involved in the redox reaction;206 A = working electrode area (cm²);207 D_0 = diffusional coefficient (cm² s⁻¹);208 C_o = analyte concentration (mol cm⁻³);209 v = scanning speed (V s⁻¹).

210

211 Pure solutions of caffeine were reacted with the zinc precursors for comparison
212 with the green synthesis. It was used a concentration of 0.05 mol L⁻¹ of zinc salt and
213 concentration of the antioxidants were determined considering a 1:4 molar ratio of Zn(II)
214 to caffeine molecules.

215

216 3.4.2 Fourier transform infrared spectroscopy (FTIR)

217 The functional groups present in the samples were determined by FTIR
218 spectroscopy (Thermo Scientific, model Nicolet iS10, Waltham, MA, United States of
219 America) using KBr pellets. The spectra were registered in a range of 4,000 to 400 cm⁻¹,

220 with a resolution of 1 cm^{-1} , using 32 scans per sample. Samples were vacuum dried at
221 $60 \text{ }^\circ\text{C}$ for 24 h, prior to the analysis to remove any possible adsorbed water.

222

223 *3.5 Characterization of ZnONPs*

224 *3.5.1 X-Ray diffraction (XRD)*

225 XRD patterns of the ZnONPs synthesized were obtained using a powder
226 diffractometer (Shimadzu, model XRD-6000, Tokyo, Japan) equipped with a Cu anode
227 ($K\alpha_1 = 1.54056 \text{ \AA}$) in a range of 2θ from 20° to 80° , with an acquisition time of 5 s. The
228 crystallite size was estimated by using the Scherrer equation [50] and the software
229 *Match!*.

230

231 *3.5.2 Field emission scanning electron microscopy (FESEM) coupled with energy* 232 *dispersive spectroscopy (EDS)*

233 ZnONPs morphology was examined with a field emission scanning electron
234 microscope (TESCAN, model MIRA 3, Brno, Czech Republic) using an energy beam of
235 15 kV and a SE detector. All the samples were placed in an aluminum stub and were
236 covered with a thin layer of gold by sputtering method (Denton Vacuum, Desk V,
237 Moorestown, NJ, United States of America) for 30 s at 0.13 mbar vacuum to perform the
238 analysis. EDS analysis was performed coupled with FESEM using a silicon drift detector
239 (SDD).

240

241 *3.5.3 Transmission electron microscopy (TEM)*

242 The particle size of synthesized ZnONPs was investigated by the analysis of
243 images obtained in a transmission electron microscope (Jeol, model JEM 1200 EX II,

244 Peabody, MA, United States of America) using a working voltage of 80 kV. The mean
245 size of the particles was determined with Image J software [51].

246

247 *3.5.4 Ultraviolet and visible spectroscopy (UV-Vis)*

248 The surface plasma resonance (SPR) and the energy band gap (E_{bg}) of the green
249 synthesized ZnONPs were evaluated by UV-Vis spectroscopy in a wavelength range of
250 250-600 nm. ZnONPs were suspended in distilled water (200 mg L⁻¹) and exposed to an
251 ultrasonic bath for 30 min. The band gap energy was obtained using the **Equation (2)**:

252

$$E_{bg} = hc / \lambda_{\max} \quad (1)$$

253

254 where,

255 h = Planck constant (6.63×10^{-34} J s);

256 c = velocity of light (2.99×10^8 m s⁻¹);

257 λ_{\max} = maximum absorption wavelength.

258

259 *3.5.5 Cell viability assay*

260 Cellular cytotoxicity was evaluated by means of the MTT method. The L929
261 strain of mouse fibroblasts were used according to the standard method described by ISO
262 10993-5[52]. Cells were cultured in DMEM, supplemented with 10% (v/v) of FBS and
263 1% (v/v) of P/S. The cultures were maintained in a humid atmosphere at 37 °C with
264 5% (v/v) CO₂. The study was performed as cells reached 70–80% confluence. Briefly,
265 cells were seeded into the 96-well plates at a density of 5.0×10^4 cells mL⁻¹. After 24 h,
266 cells were treated with different concentrations (1–80 µg mL⁻¹) of the compounds and
267 incubated for 24 h. The compounds were solubilized in DMSO. Negative controls were
268 treated with the same amounts of 0.5% (v/v) DMSO solution.

269 The medium was removed and 1.0 mg mL^{-1} MTT dye in serum-free medium was
270 added to the wells. Plates were incubated at $37 \text{ }^{\circ}\text{C}$ for 2 h in a humidified controlled
271 atmosphere with 5% (v/v) CO_2 . Subsequently, the MTT solution was removed and the
272 obtained formazan violet product was dissolved in $100 \text{ }\mu\text{L}$ DMSO for 30 min. Absorbance
273 was measured using a microplate reader (Molecular Devices, model Spectra Max 190,
274 San Jose, CA, United States of America) at 570 nm. All readings were compared with the
275 negative control, which represented 100% viability. The IC_{50} (concentration in $\mu\text{g mL}^{-1}$
276 that inhibits cell growth by 50%) was also calculated. Each experiment was performed in
277 triplicate and independently repeated at least four times.

278

279 *3.5.6 Cellular morphological analysis*

280 Mouse fibroblast cells (L929) were seeded into 24-well plates in similar
281 conditions to the cell viability analysis. After 24 h of treatment with different
282 concentrations ($1\text{--}25 \text{ }\mu\text{g mL}^{-1}$) of ZnONPs, culture medium was removed and cells were
283 prepared to FESEM and optical microscopy analyses. To perform the optical microscopy,
284 culture medium was removed after treatment and cells were dyed with Giemsa staining
285 1% (v/v). To perform FESEM analysis, after removing culture medium, cells were fixed
286 with glutaraldehyde 2% (v/v) and dehydrated with ethanol.

287

288 *3.5.7 Indirect immunofluorescence analysis*

289 L929 cells were seeded into 24-well plates containing coverslips. After 24 h
290 incubation, cells were treated with a range of different concentrations ($5\text{--}15 \text{ }\mu\text{g mL}^{-1}$) of
291 ZnONPs and incubated for 24 h. Negative controls were treated with the same amount of
292 growth medium. Positive control received rapamycin (100 nmol L^{-1}). Cells were fixed
293 with methanol at $-20 \text{ }^{\circ}\text{C}$, blocked with 2% BSA for 1 h, and incubated with the

294 monoclonal anti-LC3A/B antibody (1:100 v/v) for 1 h, followed by incubation with
 295 secondary anti-mouse fluorescein isothiocyanate (FITC) (1:150 v/v) for 1 h. The slides
 296 were mounted with coverslip and analyzed with a fluorescence light microscope
 297 (Olympus, model BX43, Miami, FL, United States of America).

298

299 **4 RESULTS AND DISCUSSION**

300

301 *4.1 Characterization of the mate leaves extract*

302 The extraction of active compounds of the *mate* leaves was optimized in terms of
 303 time and temperature, considering the antioxidant activity and total phenolic content of
 304 the plant extract. The results are presented in the Supplementary Material and the
 305 extraction time of 20 min and temperature of 50 °C was chosen to be optimal to prepare
 306 the *mate* extract for the green synthesis of ZnONPs.

307 Thus, the concentration of six main compounds present in *mate* leaves extract
 308 obtained with the optimized conditions was quantified by HPLC in both aqueous and
 309 ethanolic extracts (**Table 2**).

310

311 **Table 2** Concentration of the main *mate* compounds determined by HPLC

| Substance | Concentration ($\mu\text{g mL}^{-1}$) | |
|-------------------------|---|-------------------|
| | H ₂ O | 50% (v/v) EtOH |
| Chlorogenic acid | 42.86 \pm 0.68 | 47.96 \pm 1.27 |
| Caffeic acid | 7.18 \pm 0.02 | 7.53 \pm 0.09 |
| Caffeine | 541.39 \pm 0.72 | 654.22 \pm 0.99 |
| Theophylline | 13.22 \pm 0.35 | 28.26 \pm 0.64 |
| Theobromine | 111.00 \pm 0.92 | 125.44 \pm 0.72 |
| Rutin | n.d. | n.d. |

312 n.d. = not detected

313

314 In comparison to the aqueous extract, the 50% (v/v) ethanol extract exhibited a
 315 higher concentration of the substances evaluated, mainly for caffeine, theophylline and
 316 theobromine. This result agrees with the work of Vieira et al. [53], where ethanol
 317 increased the extraction of antioxidants substances compared to the extraction performed
 318 exclusively with water. The substance rutin, commonly found in *mate* leaves was not
 319 detected in either of the extracts with the applied methodology. Conversely to our
 320 findings, Berté et al. (2011) reported that chlorogenic acid was the main antioxidant
 321 present in the *mate* leaves, followed by caffeine and theobromine. Anesini et al.[54] have
 322 also found a major state for chlorogenic acid in commercial *mate* leaves; however, the
 323 rutin content showed to be higher than caffeine. Nonetheless, the concentration of
 324 antioxidants is significantly affected by climate, leaves age, soil characteristics, extract
 325 conditions, among others [55,56].

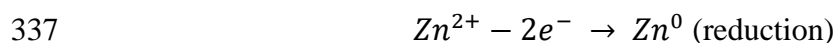
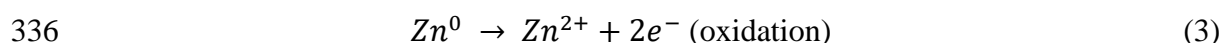
326

327 4.2 Evaluation of the green synthesis mechanism

328 4.2.1 Cyclic voltammetry

329 Cyclic voltammetry was performed in the samples Nit_EtOH, Nit_H₂O,
 330 Act_EtOH and Act_H₂O (before heat treatment) to evaluate the mechanism of formation
 331 of ZnONPs. This analysis observes change in the current when reduction or oxidation
 332 reactions occur in a system due to the transference of electrons. The cyclic voltammetry
 333 test was performed from the lowest to the highest potential, i.e., from the reduction to
 334 oxidation potential. **Equation (3)** illustrates the redox reactions for zinc:

335



338

339 Several studies support the idea that antioxidant compounds present in plants have
340 the capacity of forming complexes with or reducing metals ions [22,31,57]. Thus, if the
341 Zn(II) ions were reduced by the *mate* extract, only an oxidation peak will be visualized.
342 Conversely, if the Zn(II) ions are free in solution, both reduction and oxidation peaks will
343 be observed, and if the Zn(II) ions were complexed by the plant extract, no peak will be
344 observed as no redox reaction will take place.

345 **Figure 1** shows the voltammograms of the 50% (v/v) ethanol and aqueous extracts
346 with a concentration of 50 mg L⁻¹ in KCl 0.05 mol L⁻¹. Oxidation and reduction peaks
347 were not observed for the *mate* extract solutions in comparison to the electrolyte
348 voltammogram, which indicates that no electrochemical reaction occurred.

349 **Figure 2a** shows a typical zinc nitrate voltammogram where the peaks between
350 -0.7 V and -1.0 V are related to the oxidation-reduction reaction of Zn(II), and the peaks
351 between -1.0 and -1.25 V are related to the redox reaction of the nitrate ion, corroborating
352 with the literature [58,59]. The cyclic voltammograms of Nit_EtOH and Nit_H₂O
353 (**Figure 2b**) suggest that Zn(II) were complexed by both *mate* extracts as no peak was
354 observed in comparison to the electrolyte (KCl 0.1 mol L⁻¹).

355 Different from the samples with zinc nitrate, the samples Act_EtOH and Act_H₂O
356 (**Figures 3a** and **3b**) displayed peaks of reduction and oxidation, but with a lower current
357 than the pure zinc acetate solution. The peak current is linearly proportional to the
358 concentration of the targeted substance (Zn(II) in this case) [60]. **Figure 3c** indicates the
359 linearity relation between the peak current and zinc acetate concentration of the pure
360 solution.

361 From this relation, the concentration of zinc acetate that was reduced in the
362 Act_EtOH and Act_H₂O samples was determined as 0.041 mol L⁻¹ and 0.008 mol L⁻¹,
363 respectively, being the rest complexed by the antioxidants of the *mate* extract. Thus,

364 considering the concentration of zinc that did not undergo the redox reaction, only 71%
365 of zinc available in the sample Act_EtOH and 95% in sample Act_H₂O was possibly
366 complexed by the *mate* extract.

367 In general, Zn(II) can form coordinated complexes with nitrogen, sulfur, halogens
368 and oxygen ligands, resulting in complexes with tetrahedral (sp^3 hybridization) or
369 octahedral (sp^3d^2 hybridization) geometry, being the octahedral the less
370 thermodynamically stable form [61]. Antioxidant compounds available in plant extracts
371 usually have hydroxyl groups (from phenolic compounds) in their composition or atoms
372 with lone electrons pairs, such as nitrogen and oxygen (methylxanthines) that will form
373 metal complexes by originating an anion or by the element with a lone electron pair.

374 Methylxanthines are found in high concentrations in *mate* extracts [49,53,62].
375 Thus, the mechanism of formation of the green synthesis of ZnONPs here developed is
376 based on the molecular structure of this group and is shown in more detail in **Figure 4**.
377 According to the HPLC results, caffeine is the methylxanthines with the highest
378 concentration in the plant extract used in this study. This substance has one dissociation
379 site, where a lone pair of electrons in the nitrogen reacts to form the respective conjugated
380 acid of caffeine as indicated in **Figure 4** [63]. Besides, several studies report the formation
381 of complexes of Zn(II) and caffeine and Zn(II) and theophylline, supporting the
382 mechanism proposed here [63–67].

383 The formation of this complexes was further evaluated using pure solutions of
384 caffeine. **Figure 5** shows that the cyclic voltammograms of caffeine with zinc nitrate and
385 zinc acetate have the same pattern of the solutions prepared with the *mate* extracts,
386 confirming the involvement of this methylxanthine compound on the green synthesis of
387 ZnONPs. In addition, the analysis with zinc acetate (**Figure 5b**) also indicates that zinc

388 salt did not react completely with the antioxidant, corroborating with the results observed
389 in **Figure 3b**.

390 According to the calibration curve of zinc acetate (**Figure 3c**), approximately 60%
391 of the Zn(II) in the Act_EtOH_caffeine and 70% in the Act_H₂O_caffeine were
392 complexed by caffeine, which is lower than the concentration obtained in the analysis of
393 the green synthesis. However, the *mate* extract has different types of active compounds,
394 which might have improved the formation of complexes when using the plant extract
395 instead of the pure caffeine solution.

396

397 4.2.2 Fourier transform infrared spectroscopy

398 **Figure 6** shows the FTIR spectra of Act_EtOH_caffeine in comparison to pure
399 caffeine. Caffeine illustrates a broad and weak peak at 3460 cm⁻¹ related to the OH
400 stretching and two weak peaks at 3115 cm⁻¹ and 2950 cm⁻¹ associated with the vibration
401 of CH and CH₃ bonds. The peaks at 1700 cm⁻¹ and 1655 cm⁻¹ represent the symmetric
402 and asymmetric vibration of C=O of ketones, respectively, and a strong peak at
403 1550 cm⁻¹ indicates the presence of C=C and C=N groups. At 1240 cm⁻¹, a strong and
404 narrow peak indicates the vibration of CH bend and CN stretching. The peaks at
405 973 cm⁻¹ and 645 cm⁻¹ are associated with ring deformation while the weak peak at
406 860 cm⁻¹ is related to the wagging of CH bonds [67–69].

407 Regarding to the Act_EtOH_caffeine, a broad and strong peak at 3440 cm⁻¹ and a
408 weak peak at 2358 cm⁻¹ related to the vibration of OH indicate the presence of water in
409 the complex structure. Also, the appearance of both peaks associated with the vibration
410 of –C=O groups (1700 cm⁻¹ and 1650 cm⁻¹) indicates that complexation of Zn(II) did not
411 occur via the oxygen atom.

412

413 An analysis of specific peak areas was developed to evaluate the difference
 414 associated with the transmittance and presence of functional groups between the two
 415 substances (**Table 3**). The vibration of CH₃ (1405 cm⁻¹) was taken as a reference as the
 416 methyl groups should not be affected by the Zn(II) complexation, once they are radicals
 417 attached to the main structure of the caffeine molecule. Peak areas were taken considering
 418 the same wavenumber interval.

419 A higher Act_EtOH_caffeine ratio for the OH stretching and H₂O vibration peaks
 420 in relation to the caffeine confirms the presence of water bonded to the complex. A
 421 decrease in the peaks related to the CN group (1240 cm⁻¹ and 1023 cm⁻¹) was observed
 422 for the Act_EtOH_caffeine, indicating the complexation of the nitrogen with the Zn(II)
 423 due to a lower vibration of CN bonds. A lower ratio of ring deformation (973 cm⁻¹ and
 424 645 cm⁻¹) for the Act_EtOH_caffeine sample indicates a reduced vibration of the ring due
 425 to the formation of complexes [64]. All these findings corroborate with the complexation
 426 of the Zn (II) ions and the mechanism route for the green synthesis here proposed.

427

428 **Table 3** Ratio of peak areas of FTIR spectra of caffeine and Act_EtOH_caffeine samples

| Wavenumber (cm ⁻¹) | Peak area | | Ratio | |
|-----------------------------------|-----------|-------------------|----------|-------------------|
| | Caffeine | Act_EtOH_caffeine | Caffeine | Act_EtOH_caffeine |
| 1405 (-CH ₃) | 2551.54 | 2819.11 | – | – |
| 3460 (-OH) | 2666.18 | 13493.57 | 1.04 | 4.79 |
| 2358 (H ₂ O) | 90.62 | 277.94 | 0.04 | 0.10 |
| 1240 (-CH/-CN) | 1434.47 | 689.36 | 0.56 | 0.24 |
| 1023 (-CN) | 434.98 | 283.82 | 0.17 | 0.10 |
| 973 (rd) | 379.94 | 125.44 | 0.15 | 0.04 |
| 645 (rd) | 448.36 | 263.46 | 0.18 | 0.09 |

429 rd = ring deformation

430

431

432 The mechanism of formation was designed specifically for ZnONPs synthesized
433 with *Ilex paraguariensis* extract. However, the green synthesis of other metal oxides
434 obtained from plant extract reported in the literature probably follows the same
435 mechanistic route [46,70–72]. Likewise, the *Ilex paraguariensis* extract used in this study
436 has great potential to be applied in the production of metal and metal oxides nanoparticles
437 other the zinc oxide.

438

439 4.3 Characterization of zinc oxide nanoparticles

440 4.3.1 X-Ray diffraction (XRD)

441 XRD patterns of all samples synthesized is shown in **Figure 7**. All the peaks
442 observed correspond to *zincite* (JCPDS n° 36-1451), a hexagonal form of ZnO,
443 confirming the formation of this oxide [73]. Patterns of other crystalline structures were
444 not observed, suggesting that the nanomaterial synthesized have high purity. The average
445 crystallite size was estimated to be 19 nm for Nit_EtOH, 37 nm for Nit_H₂O, 24 nm for
446 Nit_EtOHa, 61 nm for Act_H₂O, 59 nm for Act_EtOH and 31 nm and 65 nm for
447 Control A and Control N, respectively. The lattice parameters were determined according
448 to the Bragg equation and considering all the identified planes of the hexagonal structure.
449 The parameters were found to be $a = 3.2518 \text{ \AA}$ and $c = 5.2162 \text{ \AA}$ for samples obtained
450 from zinc nitrate, and $a = 3.2564 \text{ \AA}$ and $c = 5.2166 \text{ \AA}$ for samples obtained from zinc
451 acetate, corroborating with the literature [74,75].

452

453 4.3.2 Field emission scanning electron microscopy (FESEM) coupled with energy 454 dispersive spectroscopy (EDS)

455 The surface morphology of all samples was studied by FESEM micrographs
456 (**Figures 8 and 9**). The samples produced from calcination of zinc nitrate and zinc acetate

457 (Nitrate and Acetate) showed triangular and rod particle morphology, respectively
458 (**Figures 8a–b** and **Figures 9a–b**). Samples synthesized with the green route and zinc
459 nitrate showed spherical shape (**Figures 8c–h**), while those synthesized with the green
460 route and zinc acetate have irregular shapes and sizes (**Figures 9c–f**).

461 Samples obtained with *mate* extracts and zinc nitrate have the smallest particle
462 size (**Figures 8c–h**). In addition, the synthesis with 50% (v/v) ethanol extract
463 (**Figures 8e–h**) resulted in more uniform shape and size particles than the sample obtained
464 with an aqueous extract (**Figures 8c–d**). According to the HPLC analysis, the ethanolic
465 extract has a higher concentration of antioxidants compounds, favoring the complexation
466 of Zn(II), which results in more uniform particles. The influence of calcination can be
467 evaluated from **Figures 8e–h**, where the sample Nit_EtOH (calcinated) presented more
468 homogeneous particles than the sample Nit_EtOHa (without calcination).

469 Different morphologies were observed for ZnONPs obtained by the biological
470 method using a variety of plant extracts. For instance, Nava et al. [31] obtained ZnONPs
471 from fruit peel extract and zinc nitrate with polyhedral shape. Bala et al. [35] used
472 *Hibiscus subdariffa* and zinc acetate to produce spherical ZnONPs that formed
473 agglomerates with a cauliflower shape. On the contrary, Anbuvaran et al. [5] produced
474 ZnONPs from *Phyllanthus niruri* leaves extract and zinc nitrate with irregular morphology.
475 However, the methodologies applied in each synthesis were different and a comparison
476 among the morphologies obtained is not plausible.

477 EDS results of all green synthesized ZnONPs are shown in **Figure 10**. In theory,
478 ZnO has 80.3% of Zn content. Thus, the ZnONPs synthesized from *Ilex paraguariensis*
479 extract have shown high purity with approximately 70-80% of Zn content, with exception
480 of the sample Act_H₂O that presented a lower Zn content (67%). The presence of C, O

481 and a small peak related to K can be originated from the plant compounds. Similar results
 482 were observed for ZnONPs obtained from other plant extracts [32,35].

483

484 4.3.3 Transmission electron microscopy (TEM)

485 Particle size was determined by TEM micrographs (**Figure 11**), except for the
 486 sample Nitrate because its size is greater than the size limit of analysis of a transmission
 487 electronic microscope ($\sim 1 \mu\text{m}$) and was determined by FESEM. **Table 4** shows the mean
 488 particle size for each sample. Samples green synthesized with zinc nitrate are formed by
 489 a single crystal, as the particle sizes are similar to the crystallite size determined by XRD,
 490 while the other samples are formed by several crystallites.

491

492 **Table 4** Mean size of the ZnONPs samples

| Sample | Mean size (nm) |
|-----------------------|--------------------------|
| Nitrate | $53 \pm 8 \mu\text{m}^*$ |
| Nit_H ₂ O | 33 ± 9 |
| Nit_EtOH | 18 ± 5 |
| Nit_EtOH _a | 29 ± 10 |
| Acetate | 389 ± 249 |
| Act_H ₂ O | 176 ± 50 |
| Act_EtOH | 116 ± 103 |

493 *Result is given in micrometers (μm)

494

495 Samples synthesized by green synthesis showed reduced particle size in
 496 comparison to the samples obtained from the calcination of zinc salts (Nitrate and
 497 Acetate), confirming the influence of *mate* extract to obtain ZnONPs in nanometric size.
 498 It was observed that using zinc nitrate (**Figures 11a–c**) in the green synthesis route
 499 resulted in particle sizes in the approximate range of 18 to 33 nm, which exhibited a
 500 reduction of particle size in comparison to using zinc acetate (**Figures 11d–e**). This

501 difference in the particle size possibly occurred due to the number of nucleation sites that
502 were formed during the synthesis.

503 The nucleation process is the first stage of a crystal formation in which the atoms
504 organize in a crystal structure thermodynamically stable forming the crystal nucleus from
505 where the particle grows [76]. In the case of Nitrate and Acetate, Zn(II) ions were very
506 close, resulting in fewer nucleation sites and consequently larger particle sizes.
507 Conversely, the samples Nit_EtOH, Nit_EtOHa and Nit_H₂O were complexed by the
508 antioxidants present in the *mate* extracts that kept the Zn(II) separated, originating more
509 nucleation sites and smaller particle sizes.

510 The samples Act_EtOH and Act_H₂O showed increased particle size and more
511 irregular shape than the samples Nit_EtOH, Nit_EtOHa and Nit_H₂O. This may have
512 occurred because the Zn(II) of the samples containing zinc acetate were not completely
513 complexed by the *mate* compounds as shown in the cyclic voltammetry analysis, resulting
514 in fewer nucleation sites.

515 ZnONPs obtained by plant extracts and zinc nitrate have exhibited particle sizes
516 of approximately 10 to 50 nm [5,31,35]. Nonetheless, when using zinc acetate as the metal
517 precursor, research studies have presented a contrast on the ZnONPs size that varied from
518 *quantum dots* of only 3–9 nm to clusters of 500 nm [57,77]. However, the extract
519 composition and synthesis method differ among these works and cannot be directly
520 compared.

521

522 4.3.4 Ultraviolet and visible spectroscopy (UV-Vis)

523 **Figure 12** shows the UV-Vis spectra of all green synthesized ZnONPs and their
524 respective E_{bg} . All samples showed absorption peaks between 360 and 380 nm and E_{bg}
525 around 3.3 eV characteristic of ZnONPs [78–80]. The difference between the samples

526 corroborates with the findings of Goh et al., where a decrease in particle size led to a shift
527 of the maximum absorbance to lower wavelengths and E_{bg} [81].

528

529 4.3.5 Cell viability assay

530 The cytotoxicity of ZnONPs were evaluated with L929 cells for the samples
531 Nit_ETOH, Nit_EtOHa e Nit_H₂O, as they showed reduced size and regular shape, and
532 for the sample Act_EtOH to compare the cytotoxicity of both zinc sources. Cell viability
533 for ZnONPs concentrations varying from 1–25 $\mu\text{g mL}^{-1}$ is shown in **Figure 13**.

534 Cell viability decreased with the increase of ZnONPs concentration in all samples.
535 However, the samples Nit_ETOH exhibited low cytotoxicity for concentrations varying
536 from 1 to 10 $\mu\text{g mL}^{-1}$ as cell viability was not affected in this range of concentration.
537 Syama et al. [82] also observed no cytotoxicity up to a concentration of 10 $\mu\text{g mL}^{-1}$, when
538 treating L929 cells with spherical ZnONPs ranging from 20 nm to 40 nm. Different from
539 our findings, the authors found that cell viability decreased only around 20% for samples
540 treated with 20 $\mu\text{g mL}^{-1}$ while cells treated with Nit_ETOH resulted in a decrease of around
541 50%. Paino et al. [83], by other hand, reported low levels of necrosis and apoptosis, when
542 treating the same type of cells with ZnONPs in concentrations lower than 10 $\mu\text{g mL}^{-1}$.

543 The LC₅₀ (concentration to reduce cell viability by 50%) was determined as
544 18 $\mu\text{g mL}^{-1}$ for Nit_ETOH and Act_ETOH, 9 $\mu\text{g mL}^{-1}$ for Nit_H₂O and 7 $\mu\text{g mL}^{-1}$ for
545 Nit_ETOHa. These results suggest that the samples Nit_ETOH and Act_ETOH have lower
546 cytotoxicity in comparison to the other samples. Hence, a higher concentration of
547 nanoparticle was required to reduce cell viability by 50%. On the contrary, the sample
548 Nit_ETOHa was the most cytotoxic. This sample was not calcinated which may have
549 resulted in the presence of Zn(II) species, $-\text{NO}_2^-$ and $-\text{COO}^-$ that may affect cell viability.

550 Therefore, as the sample Nit_EtOH exhibited the least cytotoxic, further analysis were
551 performed to evaluate the difference of cell viability through the different concentrations.

552

553 4.3.6 Morphological analysis of L929 cells

554 Morphological tests in L929 cells were developed with the samples (Nit_EtOH,
555 Act_EtOH, Nit_EtOHa and Nit_H₂O) to evaluate the morphological parameters with
556 Giemsa staining through optical microscopy (**Figures 14a, d, g, j and m**) and FESEM
557 (**Figures 14b, e, h, k and n**). Micrographs of both methods show similarities with
558 elongated cytoplasm in control samples (**Figures 14a, b and c**) and cytoplasmic retraction
559 and chromatin condensation points for the sample treated with Nit_EtOH (**Figures 14d,**
560 **e and f**). Other treatment conditions with Act_EtOH, Nit_EtOHa and Nit_H₂O showed
561 cellular morphology with intermediary nuclear and cytoplasmatic condensation when
562 compared to the control and Nit_EtOH samples. These results may have been related to
563 the reduced size and regular morphology of Nit_EtOH nanoparticles which can facilitate
564 the internalization of this nanomaterial into the cell, altering its biochemical and
565 morphological structure [84]. It is relevant to observe that samples exposed to Nit_EtOH
566 exhibited a cell survival *plateau* up to a maximum concentration of about 10 µg mL⁻¹,
567 displaying cytotoxicity in higher concentrations.

568 These findings corroborate with similar reports related to the cytotoxicity of ZnONPs
569 nanostructures. Syama et al. [82] observed a change from elongated to round shape after
570 treating L929 cells with ZnONPs at 50 µg mL⁻¹, whereas Satimano et al. [85] report
571 morphological changes in human A549 cells from polygonal to granules appearance, after
572 treatment with different concentrations of ZnONPs.

573

574

575 4.3.7 Indirect immunofluorescence analysis

576 Indirect immunofluorescence tests were developed in L929 cells to evaluate if the
577 morphological alterations in treated cells observed using Giemsa staining and FESEM
578 were related to autophagosome effects due to internalization and deposition of ZnONPs
579 on this vesicle. Cells were exposed to the ZnONPs (Nit_EtOH, Act_EtOH, Nit_EtOHa
580 e Nit_H₂O) for 24h with concentrations related to the LC50. An increase of LC3A/B
581 expression in cells exposed to Nit_EtOH (**Figure 14f**) was verified in comparison to
582 negative control and to cells exposed to other samples (**Figures 14c, i, l and o**).
583 Expression parameters of LC3A/B are evaluated with topographic qualitative reading in
584 the cell cytoplasm, more specifically in phagocytic regions, evidencing more intense
585 green staining for the sample treated with Nit_EtOH (LC50 concentration). All conditions
586 exhibited blue staining on the nuclear region to locate cellular structures.

587 To evaluate the LC3A/B protein expression in L929 cells exclusively to the
588 sample Nit_EtOH, a second investigation was developed with a crescent concentration
589 gradient treatment (5–15 $\mu\text{g mL}^{-1}$) with an exposure period of 24 h. This analysis showed
590 an evident increase on the LC3A/B expression after exposure to Nit_EtOH in
591 concentrations higher than 10 $\mu\text{g mL}^{-1}$ (**Figures 15e and f**). For comparison, cells were
592 exposed to a positive control (rapamycin 100 nmol L^{-1}) that exhibited LC3A/B expression
593 compatible with cells treated with high concentrations of Nit_EtOH (**Figures 15e, f and**
594 **g**). Topographical distribution using indirect immunofluorescence analysis revealed that
595 cells treated with different ZnONPs progressively increased LC3A/B expression,
596 confirming the affinity of this protein in the autophagosome of cellular structures.

597

598

599

600 5 CONCLUSIONS

601

602 ZnONPs were synthesized using *Ilex paraguariensis* leaves extract. A mechanism
603 route for the green synthesis of this nanomaterial was designed in which the antioxidants
604 of the plant extract form coordinated complexes with Zn(II) and nanoscale particles of
605 ZnO were formed via thermal degradation of these complexes. Samples obtained with
606 zinc nitrate exhibited reduced particle size and a more regular shape than those
607 synthesized with zinc acetate. These findings might be related to the fact that Zn(II)
608 present in the synthesis with zinc acetate did not react with the plant compounds in total,
609 as observed in the cyclic voltammograms.

610 Ethanol increased the extraction of active compounds from the plant resulting in
611 more uniform particles. Therefore, the sample obtained with zinc nitrate and 50% (v/v)
612 ethanol extract showed the smallest and more uniform size, which can be effective for
613 photocatalytic and biological applications.

614 Cell viability decreased with increasing of ZnONPs concentration to all samples.
615 However, sample Nit_EtOH showed no cytotoxic effects for concentrations up to a limit
616 of 10 $\mu\text{g mL}^{-1}$. Morphological analysis showed a degree of nucleus and cytoplasmic
617 condensation for cells treated with all ZnONPs samples. Small and uniform ZnONPs
618 were able to internalize cells and form deposits in phagosomes, which can initiate
619 metabolic processes of cell death in elevated concentrations. Finally, the ZnONPs
620 synthesized here can be applied in biocompatible materials in low concentrations and in
621 the development of novel therapies within the cells.

622

623

624

625 **ACKNOWLEDGMENTS**

626

627 This research was financially supported by a scholarship granted by CAPES
628 (PDSE - 88881.187620/2018-01 and 88887.153309/2017-00)

629

630 **6 REFERENCES**

- 631 [1] A.P. Reverberi, D. D.M., A.A.G. Bruzzone, R. Teti, B. Fabiano, Nanotechnology
632 in machining processes : recent advances, *Procedia CIRP*. 79 (2019) 3–8.
633 doi:10.1016/j.procir.2019.02.002.
- 634 [2] S.R.D. Mello, C.N. Cruz, M. Chen, M. Kapoor, S.L. Lee, K.M. Tyner, The
635 evolving landscape of drug products containing nanomaterials in the United States,
636 *Nat. Nanotechnol.* 12 (2017) 523–529. doi:10.1038/nnano.2017.67.
- 637 [3] F. Ye, Y. Zhao, R. El-sayed, M. Muhammed, M. Hassan, Advances in
638 nanotechnology for cancer biomarkers, *Nano Today*. 18 (2018) 103–123.
639 doi:10.1016/j.nantod.2017.12.008.
- 640 [4] R. Keçili, S. Büyüktiryaki, C. Hussain, Trends in Analytical Chemistry
641 Advancement in bioanalytical science through nanotechnology : Past , present and
642 future, *Trends Anal. Chem.* 110 (2019) 259–276. doi:10.1016/j.trac.2018.11.012.
- 643 [5] M. Anbuvaran, M. Ramesh, G. Viruthagiri, N. Shanmugam, N. Kannadasan,
644 Synthesis, characterization and photocatalytic activity of ZnO nanoparticles
645 prepared by biological method, *Spectrochim. Acta - Part A Mol. Biomol.*
646 *Spectrosc.* 143 (2015) 304–308. doi:10.1016/j.saa.2015.01.124.
- 647 [6] A. Singh, N.B. Singh, S. Afzal, T. Singh, I. Hussain, Zinc oxide nanoparticles: a
648 review of their biological synthesis, antimicrobial activity, uptake, translocation
649 and biotransformation in plants, *J. Mater. Sci.* 53 (2018) 185–201.
650 doi:10.1007/s10853-017-1544-1.

- 651 [7] V.G. Bairi, J.-H. Lim, A. Fong, S.W. Linder, Size characterization of metal oxide
652 nanoparticles in commercial sunscreen products, *J. Nanoparticle Res.* 19 (2017)
653 256. doi:10.1007/s11051-017-3929-0.
- 654 [8] S. Bhatia, N. Verma, Photocatalytic activity of ZnO nanoparticles with
655 optimization of defects, *Mater. Res. Bull.* 95 (2017) 468–476.
656 doi:10.1016/j.materresbull.2017.08.019.
- 657 [9] B. Felice, M.A. Sánchez, M.C. Socci, L.D. Sappia, M.I. Gómez, M.K. Cruz, C.J.
658 Felice, M. Martí, M.I. Pividori, G. Simonelli, A.P. Rodríguez, Controlled
659 degradability of PCL-ZnO nanofibrous scaffolds for bone tissue engineering and
660 their antibacterial activity, *Mater. Sci. Eng. C.* 93 (2018) 724–738.
661 doi:10.1016/j.msec.2018.08.009.
- 662 [10] G. Yuvaraja, J.L. Pathak, W. Zhang, Y. Zhang, X. Jiao, Antibacterial and wound
663 healing properties of chitosan/poly(vinyl alcohol)/zinc oxide beads
664 (CS/PVA/ZnO), *Int. J. Biol. Macromol.* 103 (2017) 234–241.
665 doi:10.1016/j.ijbiomac.2017.05.020.
- 666 [11] P.V. Gnaneshwar, S.V. Sudakaran, S. Abisegapriyan, J. Sherine, S. Ramakrishna,
667 M.H.A. Rahim, M.M. Yusoff, R. Jose, J.R. Venugopal, Ramification of zinc oxide
668 doped hydroxyapatite biocomposites for the mineralization of osteoblasts, *Mater.*
669 *Sci. Eng. C.* 96 (2019) 337–346. doi:10.1016/j.msec.2018.11.033.
- 670 [12] S.R. Pattabhi, A.M. Lehaf, J.B. Schlenoff, T.C.S. Keller, Human mesenchymal
671 stem cell osteoblast differentiation, ECM deposition, and biomineralization on
672 PAH/PAA polyelectrolyte multilayers, *J. Biomed. Mater. Res. - Part A.* 103 (2015)
673 1818–1827. doi:10.1002/jbm.a.35322.
- 674 [13] P.K. Mishra, H. Mishra, A. Ekielski, S. Talegaonkar, B. Vaidya, Zinc oxide
675 nanoparticles: a promising nanomaterial for biomedical applications, *Drug Discov.*

- 676 Today. 22 (2017) 1825–1834. doi:10.1016/j.drudis.2017.08.006.
- 677 [14] M. Zhai, Y. Xu, B. Zhou, W. Jing, Keratin-chitosan/n-ZnO nanocomposite
678 hydrogel for antimicrobial treatment of burn wound healing: Characterization and
679 biomedical application, *J. Photochem. Photobiol. B Biol.* 180 (2018) 253–258.
680 doi:10.1016/j.jphotobiol.2018.02.018.
- 681 [15] M. Khatami, R.S. Varma, N. Zafarnia, H. Yaghoobi, M. Sarani, V.G. Kumar,
682 Applications of green synthesized Ag, ZnO and Ag/ZnO nanoparticles for making
683 clinical antimicrobial wound-healing bandages, *Sustain. Chem. Pharm.* 10 (2018)
684 9–15. doi:10.1016/J.SCP.2018.08.001.
- 685 [16] P.P. Fu, Q. Xia, H.M. Hwang, P.C. Ray, H. Yu, Mechanisms of nanotoxicity:
686 Generation of reactive oxygen species, *J. Food Drug Anal.* 22 (2014) 64–75.
687 doi:10.1016/j.jfda.2014.01.005.
- 688 [17] C.B. Anders, J.E. Eixenberger, N.A. Franco, R.J. Hermann, K.D. Rainey, J.J.
689 Chess, A. Punnoose, D.G. Wingett, ZnO nanoparticle preparation route influences
690 surface reactivity, dissolution and cytotoxicity, *Environ. Sci. Nano.* 5 (2018) 572–
691 588. doi:10.1039/c7en00888k.
- 692 [18] P. Chen, H. Wang, M. He, B. Chen, B. Yang, B. Hu, Size-dependent cytotoxicity
693 study of ZnO nanoparticles in HepG2 cells, *Ecotoxicol. Environ. Saf.* 171 (2019)
694 337–346.
- 695 [19] A. Punnoose, K. Dodge, J.W. Rasmussen, J. Chess, D. Wingett, C. Anders,
696 Cytotoxicity of ZnO nanoparticles can be tailored by modifying their surface
697 structure: A green chemistry approach for safer nanomaterials, *ACS Sustain.*
698 *Chem. Eng.* 2 (2014) 1666–1673. doi:10.1021/sc500140x.
- 699 [20] S.R. Brintha, M. Ajitha, Synthesis and characterization of ZnO nanoparticles via
700 aqueous solution, sol-gel and hydrothermal methods, *IOSR J. Appl. Chem.* 8

- 701 (2015) 66–72. doi:10.9790/5736-081116672.
- 702 [21] A. Król, P. Pomastowski, K. Rafińska, V. Railean-Plugaru, B. Buszewski, Zinc
703 oxide nanoparticles: Synthesis, antiseptic activity and toxicity mechanism, *Adv.*
704 *Colloid Interface Sci.* 249 (2017) 37–52. doi:10.1016/j.cis.2017.07.033.
- 705 [22] O. V. Kharissova, H.V.R. Dias, B.I. Kharisov, B.O. Pérez, V.M.J. Pérez, The
706 greener synthesis of nanoparticles, *Trends Biotechnol.* 31 (2013) 240–248.
707 doi:10.1016/j.tibtech.2013.01.003.
- 708 [23] S. Shamaila, A.K.L. Sajjad, N. ul A. Ryma, S.A. Farooqi, N. Jabeen, S. Majeed, I.
709 Farooq, Advancements in nanoparticle fabrication by hazard free eco-friendly
710 green routes, *Appl. Mater. Today.* 5 (2016) 150–199.
711 doi:10.1016/j.apmt.2016.09.009.
- 712 [24] S. Iravani, Green synthesis of metal nanoparticles using plants, *Green Chem.* 13
713 (2011) 2638–2650. doi:10.1039/c1gc15386b.
- 714 [25] A. Gour, N.K. Jain, Advances in green synthesis of nanoparticles, *Artif. Cells,*
715 *Nanomedicine Biotechnol.* 47 (2019) 844–851.
716 doi:10.1080/21691401.2019.1577878.
- 717 [26] M. Bandeira, M. Giovanela, M. Roesch-Ely, D.M. Devine, J. da Silva Crespo,
718 Green synthesis of zinc oxide nanoparticles: A review of the synthesis
719 methodology and mechanism of formation, *Sustain. Chem. Pharm.* 15 (2020).
720 doi:10.1016/j.scp.2020.100223.
- 721 [27] T. Varadavenkatesan, R. Selvaraj, R. Vinayagam, Green synthesis of silver
722 nanoparticles using *Thunbergia grandiflora* flower extract and its catalytic action
723 in reduction of Congo red dye, *Mater. Today Proc.* 23 (2019) 39–42.
724 doi:10.1016/j.matpr.2019.05.441.
- 725 [28] T. Varadavenkatesan, R. Vinayagam, R. Selvaraj, Green synthesis and structural

- 726 characterization of silver nanoparticles synthesized using the pod extract of
727 *Clitoria ternatea* and its application towards dye degradation, *Mater. Today Proc.*
728 23 (2020) 27–29. doi:10.1016/j.matpr.2019.04.216.
- 729 [29] S. Anchan, S. Pai, H. Sridevi, T. Varadavenkatesan, R. Vinayagam, R. Selvaraj,
730 Biogenic synthesis of ferric oxide nanoparticles using the leaf extract of
731 *Peltophorum pterocarpum* and their catalytic dye degradation potential, *Biocatal.*
732 *Agric. Biotechnol.* 20 (2019). doi:10.1016/j.bcab.2019.101251.
- 733 [30] A. Dash, M.T. Ahmed, R. Selvaraj, Mesoporous magnetite nanoparticles synthesis
734 using the *Peltophorum pterocarpum* pod extract, their antibacterial efficacy against
735 pathogens and ability to remove a pollutant dye, *J. Mol. Struct.* 1178 (2019) 268–
736 273. doi:10.1016/j.molstruc.2018.10.042.
- 737 [31] O.J. Nava, C.A. Soto-Robles, C.M. Gómez-Gutiérrez, A.R. Vilchis-Nestor, A.
738 Castro-Beltrán, A. Olivas, P.A. Luque, Fruit peel extract mediated green synthesis
739 of zinc oxide nanoparticles, *J. Mol. Struct.* 1147 (2017) 1–6.
740 doi:10.1016/j.molstruc.2017.06.078.
- 741 [32] N. Matinise, X.G. Fuku, K. Kaviyarasu, N. Mayedwa, M. Maaza, ZnO
742 nanoparticles via *Moringa oleifera* green synthesis: Physical properties &
743 mechanism of formation, *Appl. Surf. Sci.* 406 (2017) 339–347.
744 doi:10.1016/j.apsusc.2017.01.219.
- 745 [33] C.S. Raota, A.F. Cerbaro, M. Salvador, A.P.L. Delamare, S. Echeverrigaray, J. Da
746 Silva Crespo, T.B. Da Silva, M. Giovanela, Green synthesis of silver nanoparticles
747 using an extract of Ives cultivar (*Vitis labrusca*) pomace: Characterization and
748 application in wastewater disinfection, *J. Environ. Chem. Eng.* 7 (2019) 103383.
749 doi:10.1016/j.jece.2019.103383.
- 750 [34] O.J. Nava, P.A. Luque, C.M. Gómez-Gutiérrez, A.R. Vilchis-Nestor, A. Castro-

- 751 Beltrán, M.L. Mota-González, A. Olivas, Influence of *Camellia sinensis* extract on
752 Zinc Oxide nanoparticle green synthesis, *J. Mol. Struct.* 1134 (2017) 121–125.
753 doi:10.1016/j.molstruc.2016.12.069.
- 754 [35] N. Bala, S. Saha, M. Chakraborty, M. Maiti, S. Das, R. Basu, P. Nandy, Green
755 synthesis of zinc oxide nanoparticles using *Hibiscus subdariffa* leaf extract: Effect
756 of temperature on synthesis, anti-bacterial activity and anti-diabetic activity, *RSC*
757 *Adv. 5* (2015) 4993–5003. doi:10.1039/c4ra12784f.
- 758 [36] M.M. Khan, N.H. Saadah, M.E. Khan, M.H. Harunsani, A.L. Tan, M.H. Cho,
759 Potentials of *Costus woodsonii* leaf extract in producing narrow band gap ZnO
760 nanoparticles, *Mater. Sci. Semicond. Process.* 91 (2019) 194–200.
761 doi:10.1016/j.mssp.2018.11.030.
- 762 [37] K. Singh, J. Singh, M. Rawat, Green synthesis of zinc oxide nanoparticles using
763 *Punica Granatum* leaf extract and its application towards photocatalytic
764 degradation of Coomassie brilliant blue R-250 dye, *SN Appl. Sci.* 1 (2019) 1–8.
765 doi:10.1007/s42452-019-0610-5.
- 766 [38] G. Sangeetha, S. Rajeshwari, R. Venckatesh, Green synthesis of zinc oxide
767 nanoparticles by *aloe barbadensis miller* leaf extract: Structure and optical
768 properties, *Mater. Res. Bull.* 46 (2011) 2560–2566.
769 doi:10.1016/j.materresbull.2011.07.046.
- 770 [39] S. Shahriyari Rad, A.M. Sani, S. Mohseni, Biosynthesis, characterization and
771 antimicrobial activities of zinc oxide nanoparticles from leaf extract of *Mentha*
772 *pulegium* (L.), *Microb. Pathog.* 131 (2019) 239–245.
773 doi:10.1016/j.micpath.2018.01.003.
- 774 [40] L.G. Riachi, C.A.B. De Maria, Yerba mate: An overview of physiological effects
775 in humans, *J. Funct. Foods.* 38 (2017) 308–320. doi:10.1016/j.jff.2017.09.020.

- 776 [41] E.C.S. Santos, M.A. Bicca, C.H. Blum-Silva, A.P.R. Costa, A.A. dos Santos, E.P.
777 Schenkel, M. Farina, F.H. Reginatto, T.C.M. de Lima, Anxiolytic-like, stimulant
778 and neuroprotective effects of *Ilex paraguariensis* extracts in mice, *Neuroscience*.
779 292 (2015) 13–21. doi:10.1016/j.neuroscience.2015.02.004.
- 780 [42] A.B.G. Luz, C.H.B. Da Silva, M.V.P.S. Nascimento, B.M. De Campos Facchin,
781 B. Baratto, T.S. Fröde, F.H. Reginatto, E.M. Dalmarco, The anti-inflammatory
782 effect of *Ilex paraguariensis* A. St. Hil (Mate) in a murine model of pleurisy, *Int.*
783 *Immunopharmacol.* 36 (2016) 165–172. doi:10.1016/j.intimp.2016.04.027.
- 784 [43] D. Hao, X. Gu, P. Xiao, Z. Liang, L. Xu, Y. Peng, Research progress in the
785 phytochemistry and biology of *Ilex* pharmaceutical resources, *Acta Pharm. Sin. B*.
786 3 (2013) 8–19. doi:10.1016/j.apsb.2012.12.008.
- 787 [44] F.T. Thema, E. Manikandan, M.S. Dhlamini, M. Maaza, Green synthesis of ZnO
788 nanoparticles via *Agathosma betulina* natural extract, *Mater. Lett.* 161 (2015) 124–
789 127. doi:10.1016/j.matlet.2015.08.052.
- 790 [45] A. Diallo, B.D. Ngom, E. Park, M. Maaza, Green synthesis of ZnO nanoparticles
791 by *Aspalathus linearis*: Structural & optical properties, *J. Alloys Compd.* 646
792 (2015) 425–430. doi:10.1016/j.jallcom.2015.05.242.
- 793 [46] A. Talha Khalil, S. Hameed, S. Afridi, H.E.A. Mohamed, Z.K. Shinwari, Sageretia
794 thea mediated biosynthesis of metal oxide nanoparticles for catalytic degradation
795 of crystal violet dye, *Mater. Today Proc.* (2020). doi:10.1016/j.matpr.2020.04.687.
- 796 [47] T. Yamaguchi, H. Takamura, T. Matoba, J. Terao, HPLC method for evaluation of
797 the free radical-scavenging activity of foods by using 1,1-diphenyl-2-
798 picrylhydrazyl, *Biosci. Biotechnol. Biochem.* 62 (1998) 1201–1204.
799 doi:10.1271/bbb.62.1201.
- 800 [48] V.L. Singleton, J.A. Rossi Jr., Rossi J A Jr., Colorimetry of Total Phenolics with

- 801 Phosphomolybdic-Phosphotungstic Acid Reagents, *Am. J. Enol. Vitic.* 16 (1965)
802 144–158. doi:10.12691/ijebb-2-1-5.
- 803 [49] K.A.S. Berté, M.R. Beux, P.K.W.D.S. Spada, M. Salvador, R. Ho, R.F.H. Santos,
804 Chemical Composition and Antioxidant Activity of Yerba-Mate (*Ilex*
805 *paraguariensis* A . St . -Hil ., Aquifoliaceae) Extract as Obtained by Spray Drying,
806 *J. Agric. Food Chem.* 59 (2011) 5523–5527. doi:10.1021/jf2008343.
- 807 [50] V. Uvarov, I. Popov, Metrological characterization of X-ray diffraction methods
808 at different acquisition geometries for determination of crystallite size in nano-
809 scale materials, *Mater. Charact.* 85 (2013) 111–123.
810 doi:10.1016/j.matchar.2013.09.002.
- 811 [51] C.T. Rueden, J. Schindelin, M.C. Hiner, B.E. DeZonia, A.E. Walter, E.T. Arena,
812 K.W. Eliceiri, ImageJ2: ImageJ for the next generation of scientific image data,
813 *BMC Bioinformatics.* 18 (2017) 1–26. doi:10.1186/s12859-017-1934-z.
- 814 [52] Biological evaluation of medical devices (ISO 10993-5), *Int. Organ. Stand.* (2009).
- 815 [53] M.A. Vieira, M. Maraschin, C.M. Pagliosa, R. Podestá, K.N. de Simas, I.I.
816 Rockenbach, R.D. de M.C. Amboni, E.R. Amante, Phenolic acids and
817 methylxanthines composition and antioxidant properties of mate (*Ilex*
818 *paraguariensis*) residue, *J. Food Sci.* 75 (2010) 280–285. doi:10.1111/j.1750-
819 3841.2010.01548.x.
- 820 [54] C. Anesini, S. Turner, L. Cogoi, R. Filip, Study of the participation of caffeine and
821 polyphenols on the overall antioxidant activity of mate (*Ilex paraguariensis*), *LWT*
822 - *Food Sci. Technol.* 45 (2012) 299–304. doi:10.1016/j.lwt.2011.06.015.
- 823 [55] A.C. Colpo, H. Rosa, M.E. Lima, C.E.F. Pazzini, V.B. De Camargo, F.E.M.
824 Bassante, R. Puntel, D. Ávila Silva, A. Mendez, V. Folmer, Yerba mate (*Ilex*
825 *paraguariensis* St . Hill .) -based beverages : How successive extraction influences

- 826 the extract composition and its capacity to chelate iron and scavenge free radicals
827 q, *Food Chem.* 209 (2016) 185–195. doi:10.1016/j.foodchem.2016.04.059.
- 828 [56] A.A. Esmelindro, J. dos S. Girardi, A. Mossi, J. A., C. Dariva, Influence of
829 Agronomic Variables on the Composition of Mate Tea Leaves (*Ilex paraguariensis*
830) Extracts Obtained from CO₂ Extraction at 30 ° C and 175 bar, *J. Agric. Food*
831 *Chem.* 52 (2004) 1990–1995.
- 832 [57] A.K. Singh, P. Pal, V. Gupta, T.P. Yadav, V. Gupta, S.P. Singh, Green synthesis,
833 characterization and antimicrobial activity of zinc oxide quantum dots using
834 *Eclipta alba*, *Mater. Chem. Phys.* 203 (2018) 40–48.
835 doi:10.1016/j.matchemphys.2017.09.049.
- 836 [58] M.R. Khelladi, L. Mentar, A. Beniaiche, L. Makhoulfi, A. Azizi, A study on
837 electrodeposited zinc oxide nanostructures, *J. Mater. Sci. Mater. Electron.* 24
838 (2013) 153–159. doi:10.1007/s10854-012-0973-5.
- 839 [59] N. Ait Ahmed, M. Eyraud, H. Hammache, F. Vacandio, S. Sam, N. Gabouze, P.
840 Knauth, K. Pelzer, T. Djenizian, New insight into the mechanism of cathodic
841 electrodeposition of zinc oxide thin films onto vitreous carbon, *Electrochim. Acta.*
842 94 (2013) 238–244. doi:10.1016/j.electacta.2013.01.103.
- 843 [60] A.J. Bard, L.R. Faulkner, *Electrochemical methods: fundamentals and*
844 *applications*, John Wiley & Sons, New York, 1994.
- 845 [61] J.D. Lee, *Concise inorganic chemistry*, 5th ed., Blackwell Science Ltd, Oxford,
846 1996.
- 847 [62] E.L. Cardozo, O. Ferrarese-Filho, L.C. Filho, M. de L.L. Ferrarese, C.M.
848 Donaduzzi, J.A. Sturion, Methylxanthines and phenolic compounds in mate (*Ilex*
849 *paraguariensis* St. Hil.) progenies grown in Brazil, *J. Food Compos. Anal.* 20
850 (2007) 553–558. doi:10.1016/j.jfca.2007.04.007.

- 851 [63] N. Rukk, R.S. Kusmina, Lyudmila G. Shamshiev, G.A. Davydova, E.A. Mironova,
852 A.M. Ermakov, G.A. Buzanov, A.Y. Skeyabina, A.N. Streletski, G.A. Vorobeva,
853 V.M. Retivov, P.A. Volkov, S. Belus, E. Kozhukova, V. Krasnoperova, Zinc(II)
854 and cadmium(II) halide complexes with caffeine: Synthesis, X-ray crystal
855 structure, cytotoxicity and genotoxicity studies, *Inorganica Chim. Acta.* 487 (2019)
856 184–200. doi:10.1016/j.inorg.2019.12.016.
- 857 [64] E.L.A. Mohamed, E.L.H. Hicham, Synthesis and Characterization of caffeine
858 Complexes $[M(\text{caf})_4X_2]$ $M = \text{Ni}(\text{II}), \text{Cu}(\text{II}), \text{Zn}(\text{II}), \text{Cd}(\text{II})$ $X = \text{SCN}^-$
859 $, \text{CN}^-$; caf: caffeine, *Res. J. Chem. Sci.* 4 (2014) 42–48.
- 860 [65] K. Rajam, S. Rajendran, N.N. Banu, Effect of Caffeine-Zn²⁺ System in Preventing
861 Corrosion of Carbon Steel in Well Water, *J. Chem.* 2013 (2013) 1–11.
862 doi:10.1155/2013/521951.
- 863 [66] H. Wang, T.L. Hu, R.M. Wen, Q. Wang, X.H. Bu, In vitro controlled release of
864 theophylline from metal-drug complexes, *J. Mater. Chem. B.* 1 (2013) 3879–3882.
865 doi:10.1039/c3tb20633e.
- 866 [67] H. EL Hamdani, M. EL Amane, Preparation, spectral, antimicrobial properties and
867 anticancer molecular docking studies of new metal complexes $[M(\text{caffeine})_4](\text{PF}_6)_2$; $M = \text{Fe}(\text{II}), \text{Co}(\text{II}), \text{Mn}(\text{II}), \text{Cd}(\text{II}), \text{Zn}(\text{II}), \text{Cu}(\text{II}), \text{Ni}(\text{II})$, *J. Mol. Struct.* 1184
868 (2019) 262–270. doi:10.1016/j.molstruc.2019.02.049.
- 870 [68] L. Findoráková, K. Győryová, J. Kovářová, V. Balek, F.A. Nour El-Dien, L. Halás,
871 Novel zinc(II) benzoate complex compounds with caffeine and urea synthesis and
872 characterization, *J. Therm. Anal. Calorim.* 95 (2009) 923–928.
873 doi:10.1007/s10973-008-8581-6.
- 874 [69] S.K. Srivastava, V.B. Singh, Ab initio and DFT studies of the structure and
875 vibrational spectra of anhydrous caffeine, *Spectrochim. Acta - Part A Mol. Biomol.*

- 876 Spectrosc. 115 (2013) 45–50. doi:10.1016/j.saa.2013.06.005.
- 877 [70] A.T. Khalil, M. Ovais, I. Ullah, M. Ali, Z.K. Shinwari, M. Maaza, Physical
878 properties, biological applications and biocompatibility studies on biosynthesized
879 single phase cobalt oxide (Co₃O₄) nanoparticles via *Sageretia thea* (Osbeck.),
880 Arab. J. Chem. 13 (2020) 606–619. doi:10.1016/j.arabjc.2017.07.004.
- 881 [71] N. Mayedwa, N. Mongwaketsi, S. Khamlich, K. Kaviyarasu, N. Matinise, M.
882 Maaza, Green synthesis of nickel oxide, palladium and palladium oxide
883 synthesized via *Aspalathus linearis* natural extracts: physical properties &
884 mechanism of formation, Appl. Surf. Sci. 446 (2018) 266–272.
885 doi:10.1016/j.apsusc.2017.12.116.
- 886 [72] G. Sharmila, C. Muthukumar, E. Sangeetha, Green fabrication , characterization
887 of *Pisonia alba* leaf extract derived MgO nanoparticles and its biological
888 applications, Nano-Structures & Nano-Objects. 20 (2019) 100380.
889 doi:10.1016/j.nanoso.2019.100380.
- 890 [73] M. Javed Akhtar, M. Ahamed, S. Kumar, M. Majeed Khan, J. Ahmad, S.A.
891 Alrokayan, Zinc oxide nanoparticles selectively induce apoptosis in human cancer
892 cells through reactive oxygen species, Int. J. Nanomedicine. 7 (2012) 845–857.
893 doi:10.2147/IJN.S29129.
- 894 [74] K. Rekha, M. Nirmala, M.G. Nair, A. Anukaliani, Structural , optical ,
895 photocatalytic and antibacterial activity of zinc oxide and manganese doped zinc
896 oxide nanoparticles, Phys. B Phys. Condens. Matter. 405 (2010) 3180–3185.
897 doi:10.1016/j.physb.2010.04.042.
- 898 [75] S.K.K. Shaat, H. Musleh, H. Zayed, J. Asad, N. Aldahoudi, Nano-Structures &
899 Nano-Objects Structural parameters of hydrothermally synthesized ZnO
900 nanostructure and their based solar cells, Nano-Structures & Nano-Objects. 23

- 901 (2020) 100515. doi:10.1016/j.nanoso.2020.100515.
- 902 [76] J. Meseguer, I. Pérez-Grande, A. Sanz-Andrés, Phase Change capacitors, in:
903 Spacecr. Therm. Control, 1st ed., Woodhead Publishing, Cambridge, 2012: pp.
904 209–224.
- 905 [77] G. Sathishkumar, C. Rajkuberan, K. Manikandan, S. Prabukumar, J. DanielJohn,
906 S. Sivaramakrishnan, Facile biosynthesis of antimicrobial zinc oxide (ZnO)
907 nanoflakes using leaf extract of *Couroupita guianensis* Aubl., *Mater. Lett.* 222
908 (2018) 200. doi:10.1016/j.matlet.2018.03.170.
- 909 [78] S. Pai, H. Sridevi, T. Varadavenkatesan, R. Vinayagam, Photocatalytic zinc oxide
910 nanoparticles synthesis using *Peltophorum pterocarpum* leaf extract and their
911 characterization, *Opt. - Int. J. Light Electron Opt.* 185 (2019) 248–255.
912 doi:10.1016/j.ijleo.2019.03.101.
- 913 [79] R. Vinayagam, R. Selvaraj, P. Arivalagan, T. Varadavenkatesan, Synthesis,
914 characterization and photocatalytic dye degradation capability of *Calliandra*
915 *haematocephala* -mediated zinc oxide nanoflowers, *J. Photochem. Photobiol. B*
916 *Biol.* 203 (2020) 111760. doi:10.1016/j.jphotobiol.2019.111760.
- 917 [80] S. Singh, M. Joshi, P. Panthari, B. Malhotra, A.C. Kharkwal, H. Kharkwal,
918 Citrulline rich structurally stable zinc oxide nanostructures for superior photo
919 catalytic and optoelectronic applications: A green synthesis approach, *Nano-*
920 *Structures & Nano-Objects.* 11 (2017) 1–6. doi:10.1016/j.nanoso.2017.05.006.
- 921 [81] E.G. Goh, X. Xu, P.G. McCormick, Effect of particle size on the UV absorbance
922 of zinc oxide nanoparticles, *Scr. Mater.* 78–79 (2014) 49–52.
923 doi:10.1016/j.scriptamat.2014.01.033.
- 924 [82] S. Syama, S.C. Reshma, P.J. Sreekanth, H.K. Varma, P. V. Mohanan, Effect of
925 Zinc Oxide nanoparticles on cellular oxidative stress and antioxidant defense

- 926 mechanisms in mouse liver, *Toxicol. Environ. Chem.* 95 (2013) 495–503.
927 doi:10.1080/02772248.2013.789606.
- 928 [83] I.M.M. Paino, F.J. Gonçalves, F.L. Souza, V. Zucolotto, Zinc Oxide Flower-Like
929 Nanostructures That Exhibit Enhanced Toxicology Effects in Cancer Cells, *ACS*
930 *Appl. Mater. Interfaces*. 8 (2016) 32699–32705. doi:10.1021/acsami.6b11950.
- 931 [84] K.M. Kim, M.K. Kim, H.J. Paek, S.J. Choi, J.M. Oh, Stable fluorescence
932 conjugation of ZnO nanoparticles and their size dependent cellular uptake,
933 *Colloids Surfaces B Biointerfaces*. 145 (2016) 870–877.
934 doi:10.1016/j.colsurfb.2016.06.006.
- 935 [85] M.C. Santimano, A. Martin, M. Kowshik, A. Sarkar, Zinc oxide nanoparticles
936 cause morphological changes in human A549 cell line through alteration in the
937 expression pattern of small GTPases at mRNA Level, *J. Bionanoscience*. 7 (2013)
938 300–306. doi:10.1166/jbns.2013.1134.
- 939
940
941
942
943
944
945
946
947
948
949
950

951

952

953

FIGURE CAPTIONS

954

955 **Fig. 1** Voltammograms of *mate* extracts

956

957 **Fig. 2** Cyclic voltammograms: **(a)** zinc nitrate 0.1 mol L⁻¹; **(b)** Nit_EtOH and Nit_H₂O
958 containing 0.1 mol L⁻¹ of zinc nitrate in 100 g L⁻¹ *mate* extract

959

960 **Fig. 3** Cyclic voltammogram: **(a)** zinc acetate 0.1 mol L⁻¹; **(b)** Act_EtOH and Act_H₂O
961 containing 0.1 mol L⁻¹ of zinc acetate in 100 g L⁻¹ *mate* extract; **(c)** linear relation between
962 peak current and zinc acetate concentration

963

964 **Fig. 4** ZnONPs mechanism of formation *via* green synthesis

965

966 **Fig. 5** Cyclic voltammetry of caffeine solutions reacted with **(a)** zinc nitrate and **(b)** zinc
967 acetate

968

969 **Fig. 6** FTIR spectra: **(a)** Act_EtOH_caffeine; **(b)** caffeine

970

971 **Fig. 7** XRD pattern of ZnONPs synthesized with **(a)** zinc nitrate and **(b)** zinc acetate

972

973 **Fig. 8** FESEM micrographs of ZnO synthesized from zinc nitrate: **(a-b)** Nitrate;
974 **(c-d)** Nit_H₂O; **(e-f)** Nit_EtOH; **(g-h)** Nit_EtOHa

975

976 **Fig. 9** FESEM micrographs of ZnO synthesized from zinc acetate: **(a-b)** Acetate;
977 **(c-d)** Act_H₂O; **(e-f)** Act_EtOH

978 **Fig. 10** EDS spectra of green synthesized ZnONPs

979

980 **Fig. 11** TEM micrographs of **(a)** Nit_H₂O; **(b)** Nit_EtOH; **(c)** Nit_EtOHa; **(d)** Act_H₂O;
981 **(e)** Act_EtOH; **(f)** Acetate

982

983 **Fig.12** UV- vis spectra of the green synthesized ZnONPs

984

985 **Fig. 13** L929 cell viability after treatment with ZnONPs. Samples with different letters
986 represent significant difference ($p < 0.05$)

987

988 **Fig. 14** LC3A/B expression in cells L929 after 24 h of exposure to ZnONPs (Nit_EtOH,
989 Act_EtOH, Nit_EtOHa and Nit_H₂O) with concentrations related to each IC50.

990 **a, b, c** – control samples; **d, e, f** – samples exposed to Nit_EtOH; **g, h, i** – samples exposed
991 to Act_EtOH; **j, k, l** – samples exposed to Nit_EtOHa; **m, n, o** – samples exposed to
992 Nit_H₂O.

993

994 **Fig. 15** LC3A/B expression in L929 cells after 24 h of exposure to Nit_EtOH in a crescent
995 gradient of concentration (**b** – 5 $\mu\text{g mL}^{-1}$; **c** – 7,5 $\mu\text{g mL}^{-1}$; **d** – 10 $\mu\text{g mL}^{-1}$;
996 **e** – 12,5 $\mu\text{g mL}^{-1}$; **f** – 15 $\mu\text{g mL}^{-1}$). **a** – negative control, without treatment; **g** – positive
997 control, treated with autophagy inducer rapamycin (100 nmol L^{-1}), with a cellular marker
998 pattern of LC3A/B similar to elevated concentrations of Nit_EtOH (**e, f**)

999

1000

1001

1002

1003

TABLE CAPTIONS

1004

1005 **Table 1** Description of the synthesized ZnONPs samples

1006

1007 **Table 2** Concentration of the main *mate* compounds determined by HPLC

1008

1009 **Table 3** Ratio of peak areas of FTIR spectra of caffeine and Act_EtOH_caffeine samples

1010

1011 **Table 4** Mean size of the ZnONPs samples

1012

1013

1014

1015

1016

1017

1018

1019

1020

1021

1022

1023

1024

1025

1026

1027